coatings

MDPI

Article

Quaternary Oxidized Carbon Nanohorns—Based Nanohybrid as Sensing Coating for Room Temperature Resistive Humidity Monitoring

Bogdan-Catalin Serban [1,2,*], Cornel Cobianu [1,2,3], Octavian Buiu [1,2,*], Marius Bumbac [4,5,*], Niculae Dumbravescu [1,2], Viorel Avramescu [1], Cristina Mihaela Nicolescu [5,*], Mihai Brezeanu [6], Cristiana Radulescu [4,5], Gabriel Craciun [1], Cosmin Romanitan [1] and Florin Comanescu [1]

1 National Institute for Research and Development in Microtechnologies-IMT Bucharest, 126 A Erou Iancu Nicolae Str., 077190 Voluntari, Romania; cornel.cobianu@imt.ro (C.C.); niculae.dumbravescu@imt.ro (N.D.); viorel.avramescu@imt.ro (V.A.); gabriel.craciun@imt.ro (G.C.); cosmin.romanitan@imt.ro (C.R.); florin.comanescu@imt.ro (F.C.)
2 Research Center for Integrated Systems, Nanotechnologies, and Carbon-Based Nanomaterials (CE-NASIC)-IMT Bucharest, 126 A Erou Iancu Nicolae Str., 077190 Voluntari, Romania
3 Academy of Romanian Scientists, Science, and Technology of Information Section, Str. Ilfov. Nr. 3, 050044 Bucharest, Romania
4 Sciences and Advanced Technologies Department, Faculty of Sciences and Arts, Valahia University of Targoviste, 13 Sinaia Alley, 130004 Targoviste, Romania; cristiana.radulescu@valahia.ro
5 Institute of Multidisciplinary Research for Science Technology, Valahia University of Targoviste, 13 Sinaia Alley, 130004 Targoviste, Romania
6 Faculty of Electronics, University Politehnica of Bucharest, Telecommunications and IT, 1-3 Iuliu Maniu Blvd., 6th District, 061071 Bucharest, Romania; scriemiceva@hotmail.com
* Correspondence: bogdan.serban@imt.ro (B.-C.S.); octavian.buiu@imt.ro (O.B.); marius.bumbac@valahia.ro (M.B.); cristina.nicolescu@valahia.ro (C.M.N.)

Abstract: We report the relative humidity (RH) sensing response of a resistive sensor, employing sensing layers, based on a quaternary organic–inorganic hybrid nanocomposite comprising oxidized carbon nanohorns (CNHox), graphene oxide (GO), tin dioxide, and polyvinylpyrrolidone (PVP), at 1/1/1/1 and 0.75/0.75/1/1/1 mass ratios. The sensing structure comprises a silicon substrate, a SiO_2 layer, and interdigitated transducer (IDT) electrodes. The sensing film was deposited via the drop-casting method on the sensing structure. The morphology and the composition of the sensing layers were investigated through Scanning Electron Microscopy (SEM), X-ray diffraction (XRD), and RAMAN spectroscopy. The organic–inorganic quaternary hybrid-based thin film's resistance increased when the sensors were exposed to relative humidity ranging from 0 to 100%. The manufactured devices show a room temperature response comparable to that of a commercial capacitive humidity sensor and characterized by excellent linearity, rapid response and recovery times, and good sensitivity. While the sensor with CNHox/GO/SnO_2/PVP at 0.75/0.75/1/1 as the sensing layer has the best performance in terms of linearity and recovery time, the structures employing the CNHox/GO/SnO_2/PVP at 1/1/1/1 (mass ratio) have a better performance in terms of relative sensitivity. We explained each constituent of the quaternary hybrid nanocomposites' sensing role based on their chemical and physical properties, and mutual interactions. Different alternative mechanisms were taken into consideration and discussed. Based on the sensing results, we presume that the effect of the *p*-type semiconductor behavior of CNHox and GO, correlated with swelling of PVP, dominates and leads to the overall increasing resistance of the sensing layer. The hard–soft acid–base (HSAB) principle also supports this mechanism.

Keywords: oxidized carbon nanohorns (CNHox); graphene oxide (GO); polyvinylpyrrolidone (PVP); organic–inorganic hybrid; resistive RH sensor; SnO_2; HSAB

Citation: Serban, B.-C.; Cobianu, C.; Buiu, O.; Bumbac, M.; Dumbravescu, N.; Avramescu, V.; Nicolescu, C.M.; Brezeanu, M.; Radulescu, C.; Craciun, G.; et al. Quaternary Oxidized Carbon Nanohorns—Based Nanohybrid as Sensing Coating for Room Temperature Resistive Humidity Monitoring. *Coatings* **2021**, *11*, 530. https://doi.org/10.3390/coatings11050530

Academic Editor: Dimitrios Tasis

Received: 20 March 2021
Accepted: 25 April 2021
Published: 29 April 2021

1. Introduction

Since ancient times, materials have been of cardinal importance in humanity's development and have played an essential role in human progress. According to German government estimations, around 70% of all technical innovations can be linked—to a certain extent—to the properties of the materials used [1].

Nanocomposite materials, often classified as being materials of the 21st century, have emerged as viable alternatives to overcome the limitations of traditional materials and their micro composites [2]. Among these, organic−inorganic hybrid nanocomposites have received increasing attention due to their unique physical and chemical properties. The hybrid nanostructures, developed by combining two or more nanoscaled organic and inorganic components, are a new type of composite materials with synergetic or complementary behaviors [3–5].

Organic-inorganic hybrid functional materials are considered excellent candidates in a vast number of applications in various domains such as microelectronics [6], nanomedicine [7], energy storage [8,9], light-harvesting [10], drug delivery [11], housing [12], environmental decontamination [13], gas sensors [14–16].

The research work on nanocarbonic based nanocomposites was greatly supported by international initiatives related to the field, such as Graphene Flagship (https://graphene-flagship (accessed on 26 April 2021)), with its dedicated "Graphene and Related Materials. (GRM)" section (https://graphene-flagship.eu/research/grm-projects/ (accessed on 26 April 2021)) which is presenting the national and European funding and research activities in this field. The medium and long-term impact of the knowledge accumulated and its relevance for various applications are well highlighted in recent publications [17,18].

The quaternary nanocomposites [19–21] have received considerable attention lately in line with this trend. For example, Ren et al. synthesized for the first time a quaternary nanocomposite consisting of graphene, Fe_3O_4@Fe core/shell nanoparticles, and ZnO nanoparticles [22]. The nanocomposite exhibits excellent electromagnetic absorption properties. Benedetti et al. explored the use of the quaternary nanocomposite TiO_2/CdS/rGO/Pt as a catalyst for the photocatalytic reduction of CO_2 to methane using water and visible light as the only energy sources [23]. The synthesized nanocomposites provided superior photocatalytic activity compared with the ones demonstrated by TiO_2, TiO_2/CdS binary nanocomposite, or TiO_2/CdS/Pt ternary nanocomposite. Golikand et al. developed an organic-inorganic hybrid nanocomposite based on polyaniline (PANI)/graphene nanosheets (GNS)/carbon nanotubes (CNT)/Pt [24]. The synthesized nanohybrid exhibits an outstanding average electrode specific capacity (3450 C g^{-1}) in 1M H_2SO_4 solution.

Ponnamma et al. synthesized by simple mixing method an organic-inorganic hybrid based on TiO_2 nanotubes/GO (graphene oxide)/strontium titanate ($SrTiO_3$)/poly (vinylidene fluoride-co-hexafluoropropylene [25]. Dielectric properties emphasize the energy storage capability of the synthesized nanohybrid. A quaternary hydrophilic nanohybrid was recently tested for relative humidity (RH) monitoring at room temperature [26].

On the other hand, RH sensors have received increasing attention in the last years due to their importance in a large variety of residential, industrial, and commercial applications. One can mention some of those: controlling and sensing humidity in offices and homes, medical field (gas supply infrastructure, incubators, sterilizers), food/beverage processing, chemical industry (dehumidifiers, smelting furnaces, dryers), pharmaceutical processing, electronics (semiconductor fabrication plants, clean room controls) agriculture (drip irrigation), weather station, textile, and paper industry, automotive industry (engine tests beds), etc. [27–32].

Consequently, a plethora of materials have been explored as sensing layers within the design of humidity sensors: porous silicon [33], porous polysilicon [34], silicon carbide [35], metal oxide semiconductors [36–38], conducting polymers [39,40], MoS_2 [41], polyelectrolytes [42–44], perovskites [45–47], metal-organic framework [48] and so forth. Nanocarbonic materials are widely used as sensing layers in the manufacturing of humidity sensors.

The most common nanocarbon species include: carbon nanotubes and their nanocomposites [49,50], carbon-quantum dots [51,52], fullerenes and their derivatives [53,54], graphene and its nanocomposites [55–58], carbon nanofoam [59], oxidized carbon nano-onions and their nanocomposites [60–63], graphene oxide (GO) and its nanocomposites [64,65], carbon nanohorns, oxidized carbon nanohorns (CNHox) and their nanocomposites [66–72].

The aim of the paper was to introduce a new quaternary organic-inorganic hybrid nanocomposite, i.e., CNHox/GO/SnO_2/PVP (prepared at 0.75/0.75/1/1 and 1/1/1/1 *w/w/w/w* ratios). Following the synthesis and structural characterization, we demonstrated how this new organic-inorganic hybrid nanocomposite could be used to develop a chemoresistive RH sensor and verify its room temperature functioning.

The nanocomposite structure contains four components, carefully selected, whose characteristics recommend them as constituents for the sensitive material. CNHox is characterized by high conductivity, high specific surface area/volume ratio, high affinity for water molecules [63,65,67], and GO is an excellent hydrophilic, dispersant material ideal for carbonic nanoparticles. SnO_2 nanopowder exhibits a high affinity for water molecules, good chemical stability, non-toxicity with a well-known mechanism for water vapor chemisorption [73,74]. PVP can be the polymer matrix of the sensitive layer due to its excellent binding properties with carbon nanomaterials [75].

The study presents the synthesis and structural properties of a quaternary organic-inorganic hybrid nanocomposite. The room temperature, RH sensing capabilities of these layers are further investigated, and typical characteristics (such as rise and fall times, sensitivity) are extracted.

2. Materials and Methods

2.1. Materials

All the materials described below were obtained from Sigma Aldrich (Redox Lab Supplies Com, Bucharest, Romania). The chemicals were of the highest available grade and were used as received. Details are listed below:

- Powder of CNHox (with the following linear formula $C_xH_yO_z$ and a structure shown in Figure 1a) is characterized by lengths between 40 nm and 50 nm, diameters between 2 nm to 5 nm, and specific surface area around 1300–1400 m^2/g (BET). CNHox contains 10% graphite as the main impurity and has no metal contamination.
- PVP, with the linear formula $(C_6H_9NO)_n$ and the structure depicted in Figure 1b, has an average molar weight of 10,000 Da.
- GO (15–20 sheets, 4–10% edge-oxidized, 1 mg/mL dispersion in water) has a linear formula $C_xH_yO_z$. Its structure is depicted in Figure 1c.
- Tin (IV) oxide (SnO_2) is a nanometric powder (averaged particle size lower than 100 nm), with a specific surface area around 10–25 m^2/g.
- Isopropyl alcohol, $(CH_3)_2CHOH$, is a solution 70% *w/w* in water.

2.2. Synthesis of the Quaternary Organic-Inorganic Hybrid Nanocarbonic Composites Sensing Films and Experimental Setup

For the investigation of RH sensing capabilities of the quaternary organic-inorganic hybrid nanocarbonic composites, the following chemical compositions of the sensing films were designed, synthesized, and tested: CNHox/GO/SnO_2/PVP = 1/1/1/1 and CNHox/GO/SnO_2/PVP = 0.75/0.75/1/1, both being expressed as mass ratios (*w/w/w/w*).

The dispersions' homogenization was achieved by employing a mild sonication bath (FS20D Fisher Scientific, Dreieich, Germany) at 42 kHz (output power 70 W). This process ensured a relatively uniform dispersion of the CNHox, GO, and SnO_2 in the PVP network.

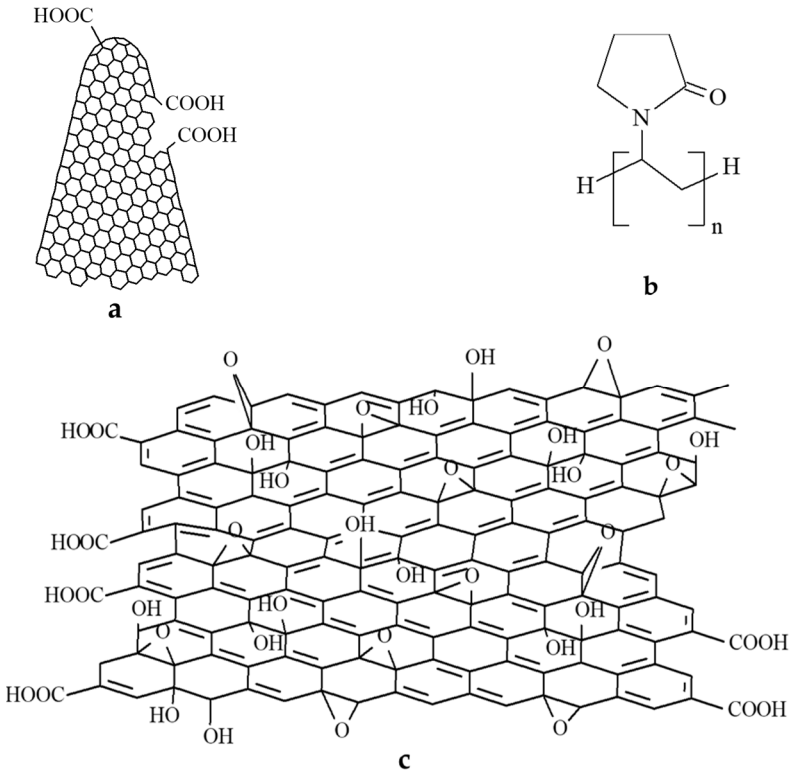

Figure 1. The structure of (**a**) CNHox, (**b**) PVP and (**c**) GO.

The synthesis of the organic-inorganic hybrid solid-state sensing films based on CNHox/GO/SnO_2/PVP = 1/1/1/1 and CNHox/GO/SnO_2/PVP = 0.75/0.75/1/1 was performed as described in the following paragraph. First, the PVP solution was prepared by dissolving 10 mg polymer in 15 mL isopropyl alcohol under stirring in the ultrasonic bath. Then, a GO dispersion in water was added to the previous PVP solution, stirred in the ultrasonic bath for 1 h at room temperature (10 mL and 7.5 mL, respectively, in 1/1/1/1 and 0.75/0.75/1/1 mixtures). CNHOx powder (10 mg and 7.5 mg, in 1/1/1/1 and 0.75/0.75/1/1 mixtures, respectively) was added to the resulted dispersion. The mixture was subjected to stirring in an ultrasonic bath for 2 h at room temperature. The nanometric SnO_2 powder, 10 mg for each sensing material, was added at the end and stirred in an ultrasonic bath for 2 h at room temperature. Finally, an annealing process was performed by heating the obtained dispersion for 24 h at 80 °C under low pressure (1 mbar). In the end, after masking the contact areas on the IDT structure, the drop-casting method was applied to obtain the sensing layers.

The sensing device consists of a metallic interdigitated (IDT) dual-comb structure fabricated on a Si substrate (470 μm thickness), covered by a SiO_2 layer (1 μm thickness) (Figure 2). The metal stripes of IDT comprise chromium (10 nm thickness) and gold (100 nm thickness) [65,67,69].

The relative humidity sensing measurements were performed in an appropriate experimental setup (Figure 3). The dry nitrogen was purged through two recipients in series containing demineralized water for varying the relative humidity in the testing chamber from 0% to 100% RH. The testing chamber included a tandem of devices: the resistive sensing structure (abbreviated as SUI–sensor under investigation) using CNHox/GO/SnO_2/PVP as sensing layers at different *w/w/w/w/*ratios, and a capacitive RH commercial sensor (COM–[76]). The latter was used to confirm the RH level indicated by the mass flow controller (MFC) system. By installing the two sensors close to each other and the gas inlet, both were exposed to the quasi-identical gas flow (wet nitrogen), thus ensuring quasi-similar experimental conditions leading to valid conclusions. A Keithley 6620 current source (Keithley Instruments GmbH, Germering, Germany), providing a recent variation between

0.01–0.1 A, was employed; the data were collected and analyzed with a PicoLog data logger (PICO Technology, Neots, Cambridgeshire, United Kingdom). All the measurements were recorded at constant room temperature [65,67,69].

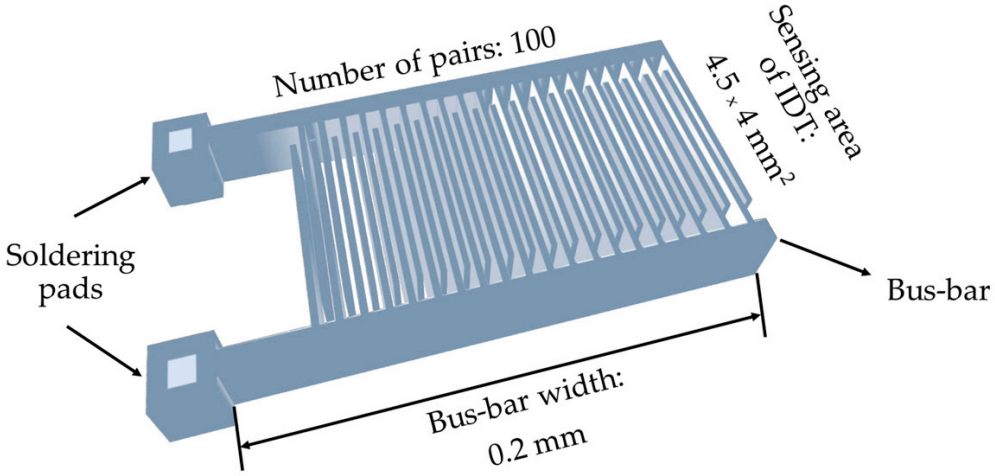

Figure 2. The layout of the sensing structure (the distance between the metallic interdigitated (IDT) dual-comb structure fingers is 10 μm).

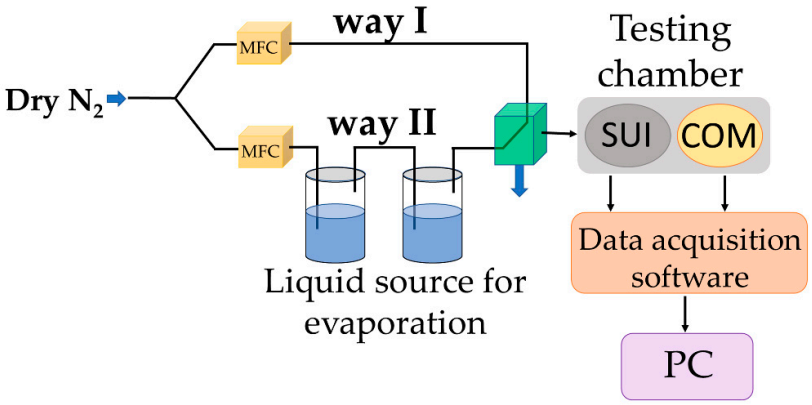

Figure 3. Experimental setup employed for RH measurements.

X-ray diffraction measurements were performed using a 9 kW Rigaku Smart Lab diffractometer (Osaka, Japan) operated at 40 kV and 75 mA. To assure a good divergence of the X-ray beam at the detector, a PSA 0.5° soller slit was used. Grazing incidence X-ray diffraction (GI-XRD) patterns were recorded keeping the incidence angle ω at 0.5°, while the detector scanned from 2θ = 5 to 60°. The peak indexing was made using the ICDD database—International Center for Diffraction Data.

The interaction between the two nanocarbon materials and PVP and SnO_2 has been proven using Raman spectroscopy. Raman spectra have been acquired by Lab Ram HR 800 Raman spectrometer (Horiba Europe, Antwerp, Belgium), using a He-Ne laser excitation (633 nm).

The surface topography of the sensing films was investigated by scanning electron microscopy (SEM). For surface visualization, a field emission gun scanning electron microscope/FEG-SEM-Nova NanoSEM 630 (Thermo Scientific, Waltham, MA, USA) (FEI), with superior low voltage resolution and high surface sensitivity imaging, was used. The investigation of the samples was made through a direct approach (no sample preparation needed); the current during the measurements was 1 nA.

3. Results and Discussion

3.1. Surface Topography

The discontinuous character of particles' distribution on the sensitive layer's surface can be observed in all recorded SEM (Figures 4 and 5). The nanoscale images show the existence of a broad particle size distribution, starting from about 10–20 nm to 100 nm, which could be correlated at least partially with the size of the crystallites identified by GIXRD (see below) and with the particle size of SnO_2 specified by the supplier Sigma-Aldrich. Also, particles of much larger dimensions (100–200 nm) can be observed due to the aggregation of particles of various sizes and crystallographic orientations.

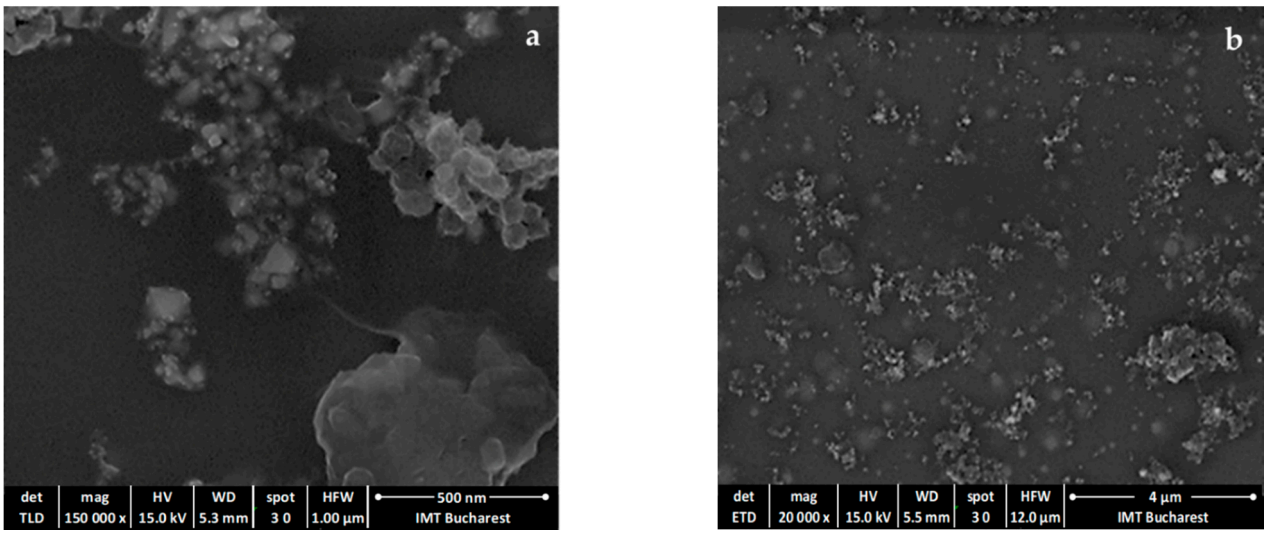

Figure 4. Scanning electron micrographs of the CNHox/GO/SnO_2/PVP = 0.75/0.75/1/1 *w/w/w/w* ratio: (**a**) magnification 150,000; (**b**) magnification 20,000.

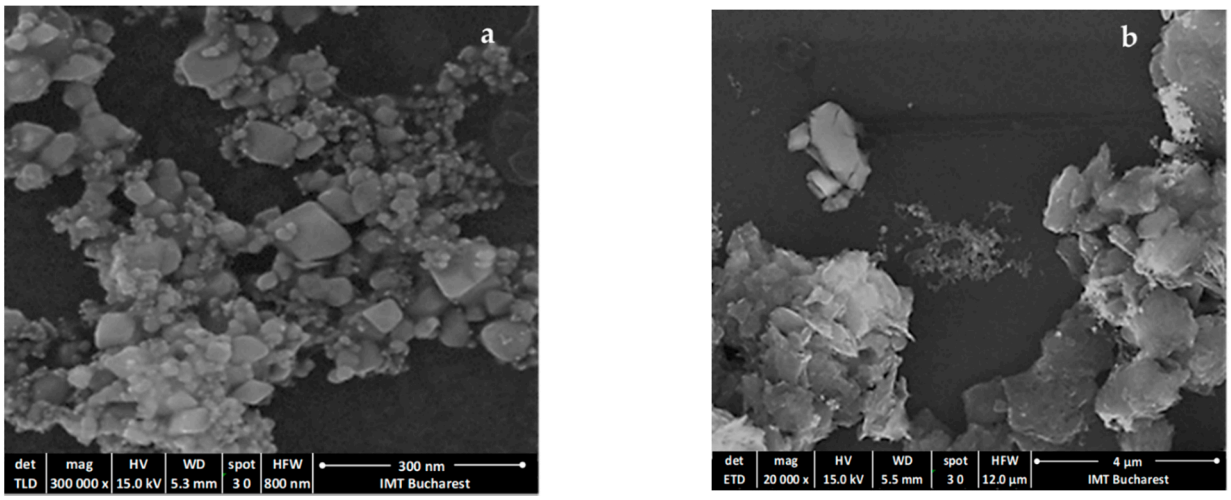

Figure 5. Scanning electron micrographs of the CNHox/GO/SnO_2/PVP = 1/1/1/1 at 1:1:1 *w/w/w/w* ratio: (**a**) magnification 300,000; (**b**) magnification 20,000.

3.2. X-ray Diffraction Results

GIXRD patterns are shown in Figure 6 for each component of quaternary organic-inorganic hybrid nanocomposite (a–d) and the organic-inorganic nanohybrid at two different *w/w/w/w* ratios (e,f).

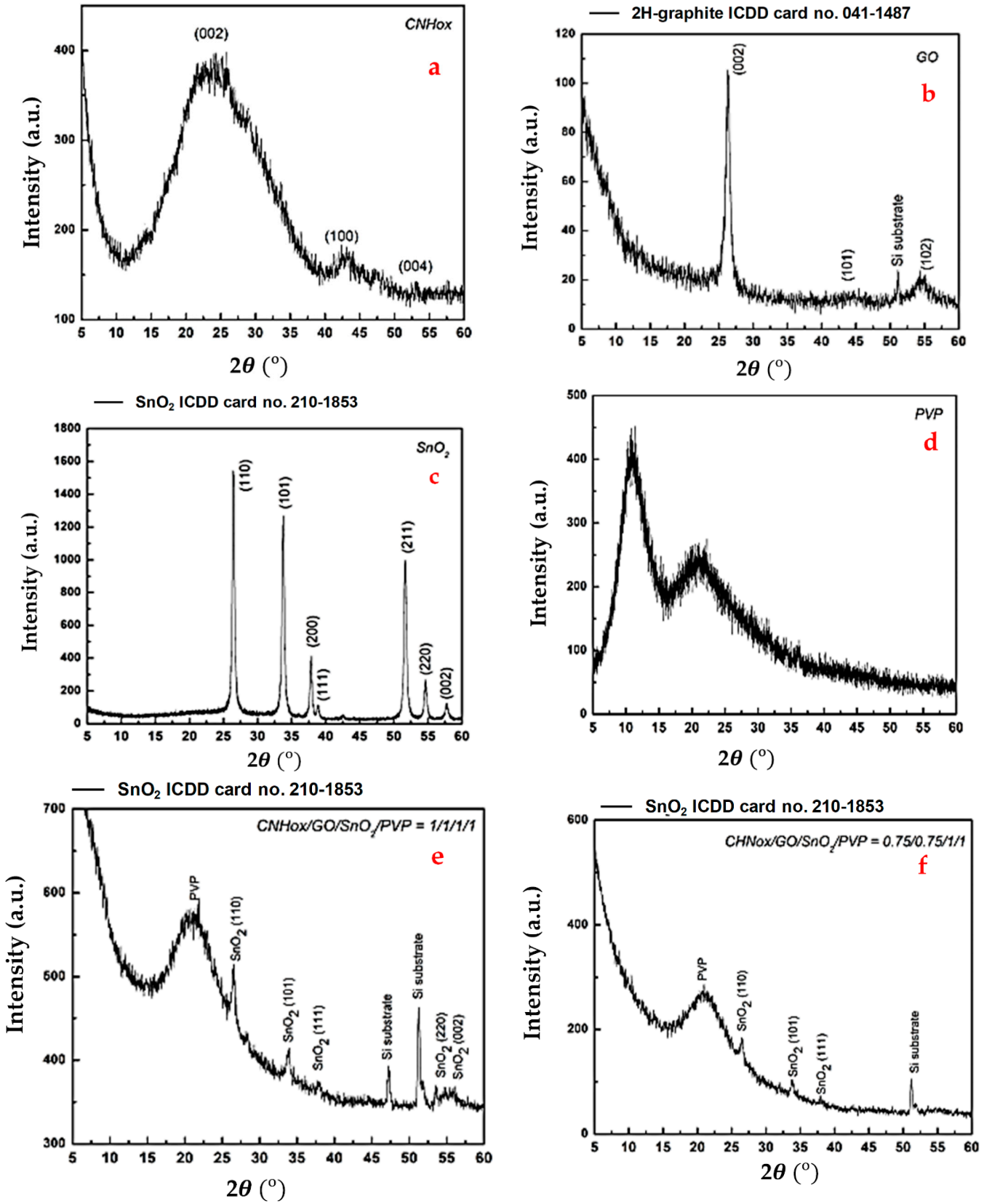

Figure 6. GIXRD pattern for (**a**) CNHox, (**b**) GO, (**c**) SnO_2, (**d**) PVP, (**e**) CNHox/GO/SnO_2/PVP = 1/1/1/1 *w/w/w/w* ratio and (**f**) CNHox/GO/SnO_2/PVP = 0.75/0.75/1/1 *w/w/w/w* ratio.

In the case of CNH (Figure 6a), the GIXRD diffraction pattern shows three broad diffraction peaks, characteristic for CNH located at 23.86°, 43.11° and 53.26°, correspondent with the (002), (100), and (004) facet of CNHs [77]. A notable exception is GO (Figure 6b), whose diffraction pattern was characteristic for graphite rather than for graphene oxide [78]. A possible explanation could be the high degree of structural defects in the commercial graphene oxide used in the design of organic-inorganic nanocomposites. In addition, a diffraction peak that comes from the Si substrate can be observed. This peak has different intensities for different samples due to different azimuthal positions (rotation angle of Si substrate) with the X-ray beam. Further, in Figure 6c, one can be observed that the GIXRD pattern exhibits multiple diffraction peaks, which can be ascribed unambiguously to wurtzite SnO_2, which belongs to 136: P42/*mnm* spatial group according to card no. 210-1853. Finally, for the latter component, the GIXRD pattern of pure PVP (Figure 6d) showed two broad characteristic peaks at 2θ = 11.25° and 21.21° corresponding to d-values of 7.96 and 4.18 Å, respectively. This is in good agreement with results reported by Li et al. [79]. If the diffractogram recorded for CNHox/GO/SnO_2/PVP at 1:1:1:1 mass ratio (Figure 6e) reveals the presence of SnO_2 with the mean crystallite size of 17.8 ± 0.89 nm, poor crystallization for SnO_2 with the mean crystallite size of 1.43 ± 0.07 nm can be estimated based on Scherrer equation [80], from the diffractogram recorded for CNHox/GO/SnO_2/PVP at 0.75:0.75:1:1 *w/w/w/w* ratio (Figure 6f). The uncertainty of the mean crystallite size was established after subtracting the instrumental broadening from the total broadening of the diffraction peak [81]. In this context, X-ray diffraction results suggest the close relationship between mass ratio and microstructural parameters.

3.3. Raman Spectroscopy

Raman spectra of quaternary nanocomposites based on CNHox/GO/SnO_2/PVP type highlighted the complexity of the chemical interactions between the four components and the nature of the multiple structural and atomic arrangement defects of the functional groups at CNHox and GO.

Thus, Figure 7a shows three Raman spectra recorded in three different positions of the film deposited from the quaternary nanocomposite CNHox/GO/SnO_2/PVP = 0.75/0.75/1/1 (*w/w/w/w*) ratio, plotted in red, green, and blue color, respectively. It can be observed that three active Raman bands (D,G,2D) were recorded at the wavenumbers of 1312, 1575.6, and 2627 cm^{-1}, which shows a redshift of these spectra by at least 10–15 cm^{-1} from the known values of the graphene oxide. One can also identify one specific SnO_2 band (635.9 cm^{-1}) having a low intensity, explainable by the small size of the related crystallites, according to the GIXRD results Figure 6. The displacement of the Raman peak positions of the carbonaceous material is the most spectacular result in Figure 7. Besides, it is well known from the literature that there are significant differences between the scattering maxima of graphene oxide reported by different authors [82,83]. This spectrum's specific features can be explained by the presence of chemical interaction (stacking interactions and hydrogen bond between GO and CNHox) and the high density of defects in GO, as revealed in the previous XRD analysis performed on the different GO material. In the same vein, Figure 7b shows the Micro-Raman spectra of the film with the quaternary composition CNHox/GO/SnO_2/PVP = 1/1/1/1. According to the Raman spectrum of pure PVP, the weak band at 1606, 9 cm^{-1} can be attributed to the PVP [83]. The very weak band around 2450 cm^{-1} can originate from the double resonance process involving the phonon dispersion of two-dimensional graphite (a major impurity of oxidized carbon nanohorn) [84].

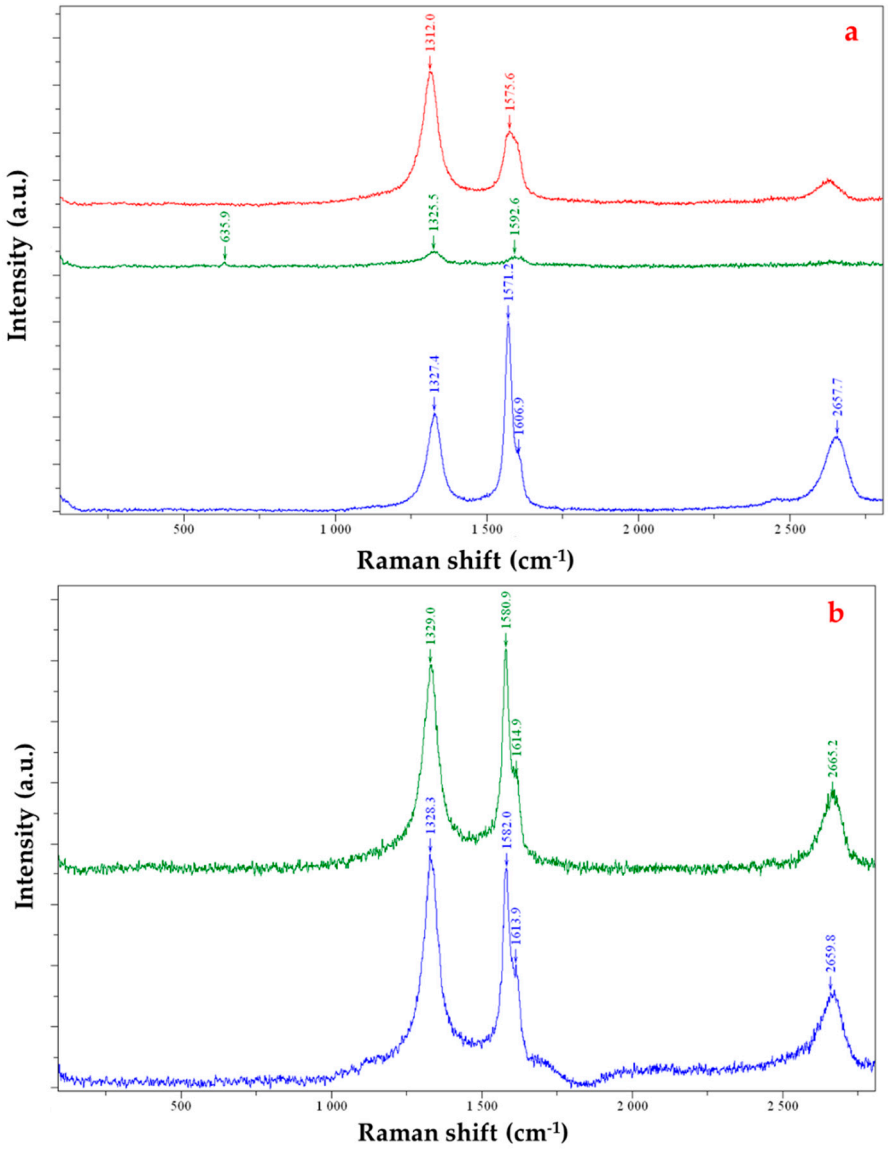

Figure 7. Raman spectra of solid-state films of (**a**) CNHox/GO/SnO_2/PVP = 0.75/0.75/1/1 (mass ratio) deposited on a silicon substrate (three different measuring points of the film deposited from the quaternary nanocomposite-red, green, and blue curves), and (**b**) CNHox/GO/SnO_2/PVP = 1/1/1/1 (mass ratio) deposited on a silicon substrate (two different measuring points—green and blue curves).

3.4. RH Monitoring Capability of the Quaternary Nanocomposite

The RH monitoring capability of each organic-inorganic hybrid nanocomposite–based sensing layer was explored by applying a current between the two electrodes and measuring the voltage difference when varying the RH from 0% to 100%. To simplify the analysis, the following abbreviations will be used:

- sensor 0.75—a resistive sensor that employed a sensing layer based on CNHox/GO/SnO_2/ PVP at 0.75/0.75/1/1 mass ratio.
- sensor 1.0—a resistive sensor that used a sensing layer based on CNHox/GO/SnO_2/PVP at 1/1/1/1 mass ratio.

A notable characteristic of these sensors is low power consumption, below 2 mW. The behavior of the manufactured sensors is presented below (Figure 8a,b):

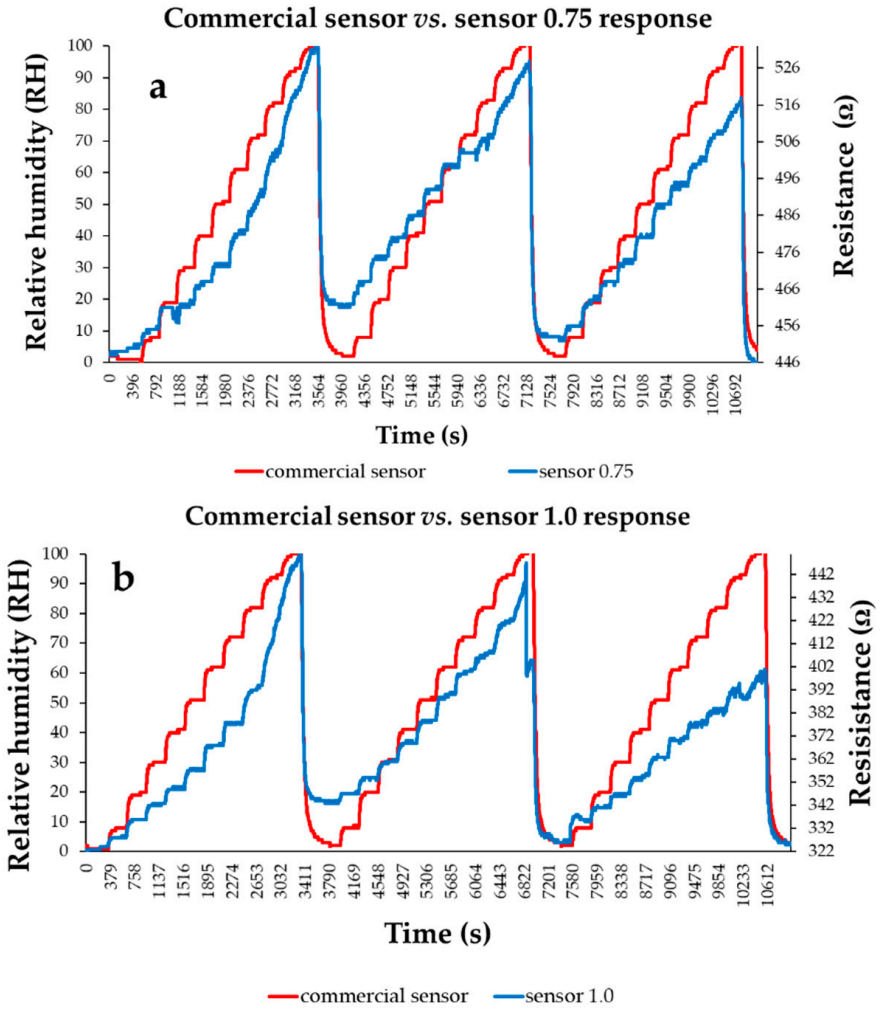

Figure 8. The response of (**a**) Sensor 0.75 and (**b**) Sensor 1.0. "R curve-blue" presented as a function of time for three measurement cycles when relative humidity was increased in ten steps from 0% RH to 100% RH; "RH curve-red" shows similar characteristic measured for a commercial, capacitive sensor.

The resistance of the organic-inorganic quaternary hybrid-based thin film increases when RH increases. It is observed that the resistance of the sensing layer for the RH value "0" is growing with the decrease of the CNHox (nanocarbonic materials with high conductivity) content in the nanohybrid. The quaternary nanohybrid-based resistive sensors' overall linearity—in humid nitrogen when varying RH from 0% to 100%—is excellent, as shown in Figure 9. In terms of linearity, the sensor 0.75 seems to have better performance (R^2 = 0.99).

Two important parameters, such as response time and recovery time (in seconds), were calculated for both manufactured RH resistive sensors. If R(t) is the response of the device in time, the t_r can be evaluated as:

$$t_r = t_{90} - t_{10} \quad (1)$$

where t_{90} and t_{10} represent the moments when the response R(t) reaches 90% and 10%, respectively, from the total variation of the sensor's resistance due to a change in the RH value (as in the example presented in Figure 10).

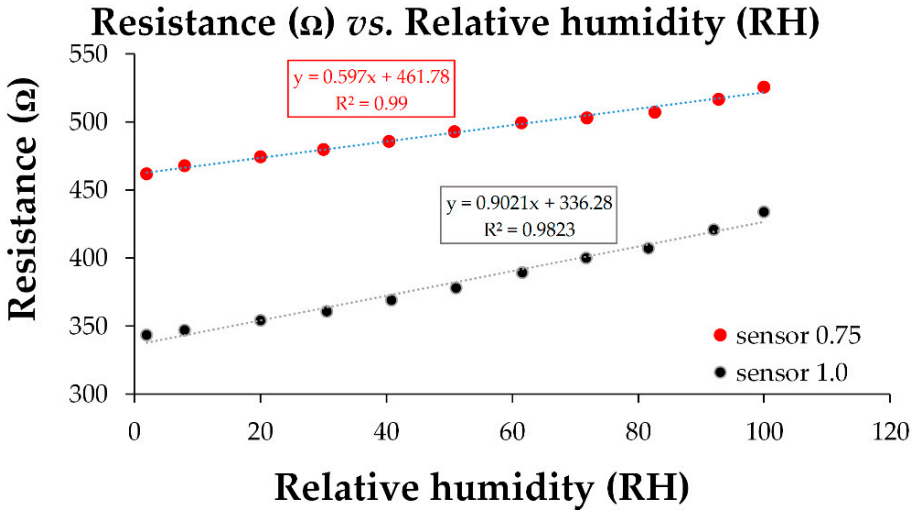

Figure 9. The transfer function of the quaternary nanohybrid-based resistive sensors in humid nitrogen (RH = 0–100%).

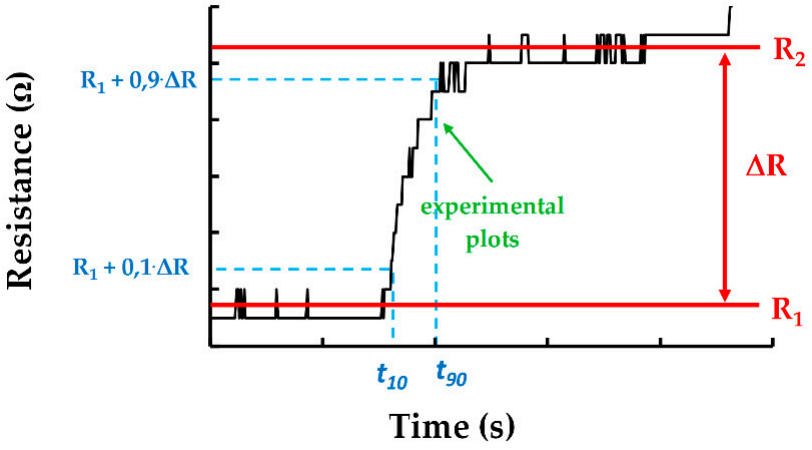

Figure 10. Example for the calculation of response time.

For the RH variation from 40 to 50% (Figure 11a,b), the response times of sensor 0.75, sensor 1.0, and commercial sensors are 43, 42, and 37(31), respectively. However, it was observed that for lower humidity values (up to 30% RH), the response time of the commercial sensor is higher compared to sensor 1.0. A similar situation was recorded for the RH variation from 60 to 70%.

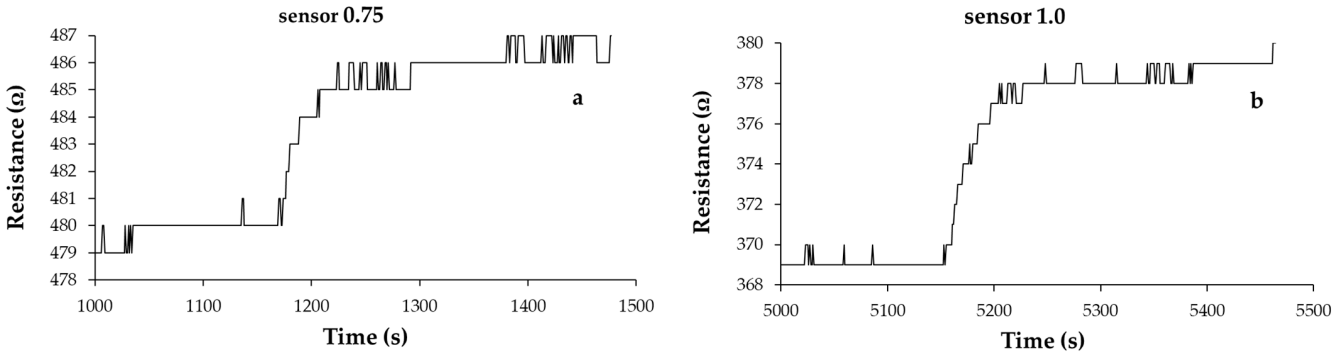

Figure 11. Response time of the RH resistive at room temperature for 40% RH–50% RH step: (**a**) sensor 0.75 and (**b**) sensor 1.0.

On the other hand, higher response times were obtained for the entire RH range for sensor 0.75 compared to sensor 1.0. This result can be explained by decreasing the number of active sites when the concentrations of CNHox and GO decrease in the sensing layer.

At the same time, higher response times were calculated at RH levels higher than 70% compared with values for response time for RH values below 50%. This result can be explained by the saturation of actives sites at high relative humidity, a process that is further detailed. Water molecules penetrate the hydrophilic organic-inorganic hybrid sensing film. Due to hydrophilic constituents' presence, the hybrid nanocomposite film adsorbs/absorbs a substantial amount of water (related to the sensing film's mass). Finally, some water molecules can condensate in the proximity of hydrophilic groups, thus blocking active sites.

Similarly, the recovery times are calculated (see the examples in Figure 12a,b).

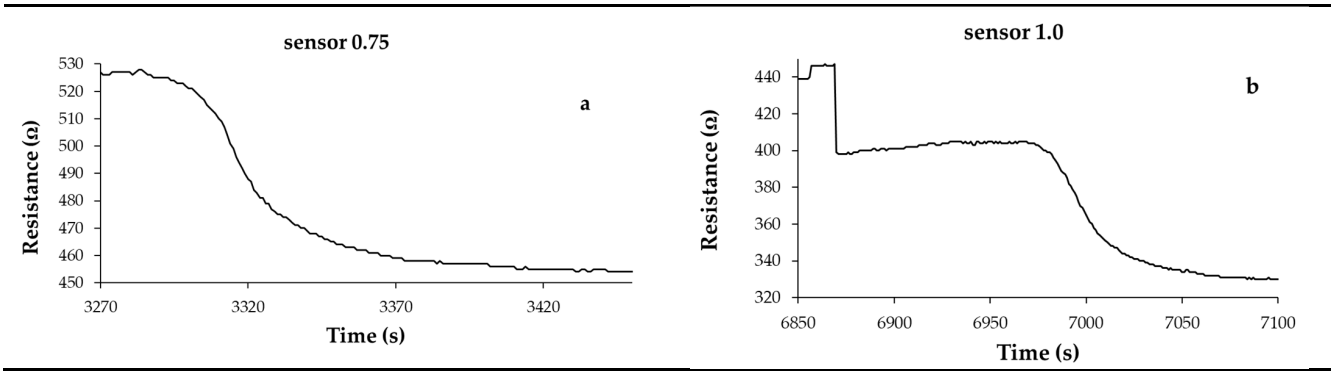

Figure 12. Recovery times of the resistive sensor after the second cycle; the recovery time was measured from 100% to 0% RH (clean, dry nitrogen): (**a**) sensor 0.75 and (**b**) sensor 1.0.

Sensor 0.75 has a better performance in terms of recovery time than the commercial sensor and sensor 1.0. Sensor 0.75 has a recovery time of 72 s, while sensor 1.0 has a recovery time of 164 s.

To compare the sensing performances of both manufactured RH resistive sensors, a relative sensitivity (S_r) was defined. This S_r value consists of sensitivity ($S = \Delta R/\Delta RH$) of the transfer characteristic from Figure 10 divided by the sensor's initial electrical resistance in clean, dry nitrogen (R_0). These results are presented in Table 1 for the second cycle of functioning of the sensors. As can be observed, sensor 1.0 exhibits the best performance.

Table 1. Sensing parameters for 0.75 and 1.0 RH resistive sensors.

Sensor Parameters	Sensor Type	
	Sensor 0.75	**Sensor 1.0**
Resistance, Ro [Ω]	461.78	336.28
Sensitivity, $S = \Delta R/\Delta RH$	0.5970	0.9021
Relative sensitivity, $S_r = S/R0$	0.00129	0.00268

3.5. Analysis of Sensing Mechanism

Each constituent of the quaternary organic-inorganic hybrid nanocomposite employed for resistive monitoring of RH has a specific role. CNHox shows appropriate features such as increased conductivity, high specific surface area/volume ratio, an affinity for water molecules, as well, as a rapid variation of the electrical resistance in contact with a water molecule in the humidity range from 0% RH to 100% RH, available in high purity, and last but not least, facile synthesis. All these outstanding properties make CNHox a valuable candidate for monitoring resistive room temperature RH [63,65,67].

GO exhibits many advantages such as superior hydrophilic properties, good charge carrier, suitable dispersant for carbonic nanoparticles such as carbon nanotubes or carbon

nanohorns, possibility to modulate chemical and physical properties through covalent and noncovalent functionalization, excellent mechanical properties [73]. Furthermore, due to oxygen functionalities, GO shows excellent dispersibility in water and different organic solvents.

SnO_2 powder exhibits good sensitivity towards relative humidity, high chemical stability, non-toxicity, and low-cost synthesis [74].

PVP is a hydrophilic polymer with excellent binding properties [75].

Taking into consideration the possible interactions between water and the above-listed materials, four distinct sensing mechanisms can be identified and analyzed:

- The high proton conductivity of GO and CNHox.

This approach is related to the dissociation of water and ionization of carboxylic groups. The adsorbed water molecules on CNHox and GO hydrophilic surfaces may dissociate to H^+ and OH^- ions. Besides, carboxylic groups found in the molecular architecture of both nanocarbonic materials may dissociate. The generated proton may tunnel from one water molecule to another through hydrogen bonding, increasing the overall electrical conductivity of the organic-inorganic hybrid-based sensing film [85].

- Water acting as an electrons donor for *p*-type semiconducting materials such as CNHox and GO [86].

The second mechanism takes into consideration the *p*-type semiconducting material properties of both CNHox and GO. At the interaction with nanocarbonic materials, H_2O molecules donate their electron pairs, decreasing the number of holes in GO and CNHox. Consequently, the humidity sensing layer based on quaternary hybrid nanocomposite should become more resistive.

One can also judge this mechanism from the perspective of the hard-soft acid-base (HSAB) principle. Thus, according to HSAB, in the sensing process, water molecules classified as hard Lewis bases will interact with the holes of the *p-type* semiconducting materials CNHox and GO (which can be virtually categorized as strong Lewis acids). Therefore, they will be nulling each other by multiple recombination processes [87–89].

- The swelling of the dielectric, hydrophilic polymer.

PVP is a dielectric polymer with hydrophilic properties, and therefore prone to swelling due to interaction with water molecules. Thus, the distances between GO and CNHox nanoparticles increase, electrically percolating pathways being diminished. According to this approach, the sensitive layer should become more resistive [90].

- The release of electrons from the interaction of SnO_2-H_2O.

In general, water molecules can be adsorbed by physisorption or hydrogen bonding and react with the Lewis acid site and Lewis base site on the SnO_2 surface, thus releasing electrons (e^-) [91]. According to this approach, the sensitive layer should become more conductive.

As shown in Figure 10, the resistive test structure's transfer characteristics demonstrate that the values of electrical resistance as a function of RH level increase. These results suggest that the overall behavior of the quaternary organic-inorganic hybrid nanocomposites CNHox/GO/SnO_2/PVP = 1/1/1/1 and CNHox/GO/SnO_2/PVP = 0.75/0.75/1/1 is equivalent to a *p*-type semiconducting material behavior.

It is reasonable to accept that adding SnO_2 to the CNHox and GO will result in the formation, in the quaternary nanocomposite, of islands of *p-n* semiconductor heterojunctions embedded in the PVP (as dielectric material). The behavior of the sensing layer indicates that heterostructures built between *n*-type SnO_2 and *p*-type CNHox and GO may not play a cardinal role in the electrical conduction. Therefore, the RH monitoring process could be explained by the presence of the percolating paths of CNHox (significant contribution) and GO (minor contribution), that shunt the *p-n* heterojunctions, which ultimately could influence only the geometry of the conducting pathways of the quaternary hybrid. In other words, it may be assumed that effect of the *p*-type semiconductor behavior of CNHox

and GO correlated with swelling of PVP dominates and leads to the overall increasing resistance of the sensing layer.

4. Conclusions

In this study, an RH sensing response of resistive sensors, employing sensing layers, based on an organic–inorganic quaternary hybrid nanocomposite comprising CNHox/GO/SnO_2/PVP = 1/1/1/1 and CNHox/GO/SnO_2/PVP = 0.75/0.75/1/1 mass ratios, was reported. The manufactured sensors show a room temperature response comparable to that of a commercial capacitive humidity sensor. They are characterized by excellent linearity, rapid response and recovery times, and good sensitivity. While the sensor with CNHox/GO/SnO_2/PVP at 1/1/1/1 (mass ratio) as the sensing layer has the best performance in terms of relative sensitivity and response time, the structure employing the CNHox/GO/SnO_2/PVP at 0.75/0.75/1/1 (mass ratio) has better performance regarding the linearity and recovery time. We highlighted that the role of each component of the quaternary hybrid nanocomposites in the sensing was explained based on their chemical and physical properties, and mutual interactions. Four sensing mechanisms were taken into account and discussed. Based on the sensing results, the *p*-type semiconductor behavior of CNHox and GO, in conjunction with swelling of PVP, prevails and leads to the overall increasing resistance of the sensing films. The hard–soft acid–base (HSAB) theory also supports this interpretation.

The low power consumption of the manufactured sensors, below 2 mW, and the sensing performances at room temperature and manufacturing simplicity are the essential benefits of the presented sensors.

5. Patents

The IMT authors would like to acknowledge the financial support provided by the Romanian Ministry of Education and Research, via the "Nucleu Program" known as "MICRO-NANO-SIS PLUS", grant number PN 19 16, and the UEFISCDI contract no 364PED-23.10.2020.

Author Contributions: Conceptualization, B.-C.S., C.C. and O.B.; methodology, B.-C.S., C.C., V.A., G.C., N.D., O.B. and C.R. (Cristiana Radulescu); software, M.B. (Marius Bumbac), C.M.N. and M.B. (Mihai Brezeanu); validation, B.-C.S., C.C., N.D., O.B., F.C., C.R. (Cosmin Romanitan), M.B (Mihai Brezeanu) and C.R. (Cristiana Radulescu); investigation, N.D., B.-C.S., V.A., G.C., C.C., C.R. (Cosmin Romanitan) and F.C.; resources, M.B. (Marius Bumbac), C.M.N. and C.R. (Cristiana Radulescu); writing—original draft preparation, B.-C.S., C.C., O.B. and M.B. (Mihai Brezeanu).; writing—review and editing, all co-authors; visualization, O.B.; supervision, B.-C.S., C.C. and M.B. (Marius Bumbac).; project administration, B.-C.S. and O.B.; funding acquisition, O.B. and M.B. (Marius Bumbac). All authors have read and agreed to the published version of the manuscript.

Funding: IMT authors would like to acknowledge the financial support provided by the Romanian Ministry of Education and Research, via the "Nucleu Program" called "MICRO-NANO-SIS PLUS", grant number PN 19 16, and the UEFISCDI contract no 364PED-23.10.2020.

Data Availability Statement: The data presented in this study are available within the present article.

Conflicts of Interest: The authors declare no conflict of interest. The funders had no role in the design of the study; in the collection, analyses, or interpretation of data; in the writing of the manuscript, or in the decision to publish the results.

References

1. Malik, S.; Krasheninnikov, A.V.; Marchesan, S. Advances in nanocarbon composite materials. *Beilstein J. Nanotechnol.* **2018**, *9*, 20–21. [CrossRef] [PubMed]
2. Camargo, P.H.C.; Satyanarayana, K.G.; Wypych, F. Nanocomposites: Synthesis, structure, properties and new application opportunities. *Mater. Res.* **2009**, *12*, 1–39. [CrossRef]
3. Kaushik, A.; Kumar, R.; Arya, S.K.; Nair, M.; Malhotra, B.D.; Bhansali, S. Organic–inorganic hybrid nanocomposite-based gas sensors for environmental monitoring. *Chem. Rev.* **2015**, *115*, 4571–4606. [CrossRef]

4. Zhao, N.; Yan, L.; Zhao, X.; Chen, X.; Li, A.; Zheng, D.; Xu, F.J. Versatile types of organic/inorganic nanohybrids: From strategic design to biomedical applications. *Chem. Rev.* **2018**, *119*, 1666–1762. [CrossRef]
5. Sreejith, S.; Huong, T.T.M.; Borah, P.; Zhao, Y. Organic–inorganic nanohybrids for fluorescence, photoacoustic and Raman bioimaging. *Sci. Bull.* **2015**, *60*, 665–678. [CrossRef]
6. Huang, Q.R.; Volksen, W.; Huang, E.; Toney, M.; Frank, C.W.; Miller, R.D. Structure and interaction of organic/inorganic hybrid nanocomposites for microelectronic applications. 1. MSSQ/P (MMA-co-DMAEMA) nanocomposites. *Chem. Mater.* **2002**, *14*, 3676–3685. [CrossRef]
7. Hayashi, K.; Maruhashi, T.; Sakamoto, W.; Yogo, T. Nanomedicine: Organic–Inorganic Hybrid Hollow Nanoparticles Suppress Oxidative Stress and Repair Damaged Tissues for Treatment of Hepatic Fibrosis. *Adv. Funct. Mater.* **2018**, *28*, 1870086. [CrossRef]
8. Wei, Z.; Almakrami, H.; Lin, G.; Agar, E.; Liu, F. An organic-inorganic hybrid photoelectrochemical storage cell for improved solar energy storage. *Electrochim. Acta* **2018**, *263*, 570–575. [CrossRef]
9. Zhao, X.; Li, Z.; Guo, Q.; Yang, X.; Nie, G. High performance organic-inorganic hybrid material with multi-color change and high-energy storage capacity for intelligent supercapacitor application. *J. Alloys Compd.* **2021**, *855*, 157480. [CrossRef]
10. Chen, C.H.; Liu, K.Y.; Sudhakar, S.; Lim, T.S.; Fann, W.; Hsu, C.P.; Luh, T.Y. Efficient Light Harvesting and Energy Transfer in Organic− Inorganic Hybrid Multichromophoric Materials. *J. Phys. Chem. B* **2005**, *109*, 17887–17891. [CrossRef]
11. Ilhan-Ayisigi, E.; Yesil-Celiktas, O. Silica-based organic-inorganic hybrid nanoparticles and nanoconjugates for improved anticancer drug delivery. *Eng. Life Sci.* **2018**, *18*, 882–892. [CrossRef]
12. Xu, Q.; Li, X.; Jin, Y.; Sun, L.; Ding, X.; Liang, L.; Wang, B. Bacterial self-defense antibiotics release from organic–inorganic hybrid multilayer films for long-term anti-adhesion and biofilm inhibition properties. *Nanoscale* **2017**, *9*, 19245–19254. [CrossRef]
13. Yi, F.Y.; Zhu, W.; Dang, S.; Li, J.P.; Wu, D.; Li, Y.H.; Sun, Z.M. Polyoxometalates-based heterometallic organic–inorganic hybrid materials for rapid adsorption and selective separation of methylene blue from aqueous solutions. *Chem. Commun.* **2015**, *51*, 3336–3339. [CrossRef] [PubMed]
14. Rebber, M.; Willa, C.; Koziej, D. Organic–inorganic hybrids for CO_2 sensing, separation and conversion. *Nanoscale Horiz.* **2020**, *5*, 431–453. [CrossRef] [PubMed]
15. Bai, S.; Zhang, K.; Sun, J.; Zhang, D.; Luo, R.; Li, D.; Liu, C. Polythiophene-WO_3 hybrid architectures for low-temperature H_2S detection. *Sens. Actuators B Chem.* **2014**, *197*, 142–148.
16. Jayachandiran, J.; Arivanandhan, M.; Padmaraj, O.; Jayavel, R.; Nedumaran, D. Investigation on ozone-sensing characteristics of surface sensitive hybrid rGO/WO_3 nanocomposite films at ambient temperature. *Adv. Compos. Hybrid. Mater.* **2020**, *3*, 16–30. [CrossRef]
17. Döscher, H.; Reiss, T. Graphene Roadmap Briefs (No. 1): Innovation interfaces of the Graphene Flagship. *2D Mater.* **2021**, *8*, 022004. [CrossRef]
18. Döscher, H.; Schmaltz, T.; Neef, C.; Thielmann, A.; Reiss, T. Graphene Roadmap Briefs (No. 2): Industrialization status and prospects. *2D Mater.* **2021**, *8*, 022005. [CrossRef]
19. Wang, L.; Huang, Y.; Ding, X.; Liu, P.; Zong, M.; Sun, X.; Zhao, Y. Supraparamagnetic quaternary nanocomposites of graphene@ Fe_3O_4@ SiO_2@ SnO_2: Synthesis and enhanced electromagnetic absorption properties. *Mater. Lett.* **2013**, *109*, 146–150. [CrossRef]
20. Huang, Q.; Wei, W.; Yan, Q.; Wu, C.; Zhu, X. A facile and green method for synthesis of rGO@SiO_2@FeOOH@ Ag nanocomposite as efficient surface enhanced Raman scattering (SERS) platforms. *Mater. Lett.* **2015**, *152*, 203–206. [CrossRef]
21. Divya, K.S.; Xavier, M.M.; Vandana, P.V.; Reethu, V.N.; Mathew, S. A quaternary TiO_2/ZnO/RGO/Ag nanocomposite with enhanced visible light photocatalytic performance. *N. J. Chem.* **2017**, *41*, 6445–6454.
22. Ren, Y.L.; Wu, H.Y.; Lu, M.M.; Chen, Y.J.; Zhu, C.L.; Gao, P.; Ouyang, Q.Y. Quaternary nanocomposites consisting of graphene, Fe_3O_4@Fe core@ shell, and ZnO nanoparticles: Synthesis and excellent electromagnetic absorption properties. *ACS Appl. Mater. Interfaces* **2012**, *4*, 6436–6442. [CrossRef]
23. Benedetti, J.E.; Bernardo, D.R.; Morais, A.; Bettini, J.; Nogueira, A.F. Synthesis and characterization of a quaternary nanocomposite based on TiO_2/CdS/rGO/Pt and its application in the photoreduction of CO_2 to methane under visible light. *RSC Adv.* **2015**, *5*, 33914–33922. [CrossRef]
24. Golikand, A.N.; Bagherzadeh, M.; Shirazi, Z. Evaluation of the polyaniline based nanocomposite modified with graphene nanosheet, carbon nanotube, and Pt nanoparticle as a material for supercapacitor. *Electrochim. Acta* **2017**, *247*, 116–124. [CrossRef]
25. Ponnamma, D.; Erturk, A.; Parangusan, H.; Deshmukh, K.; Ahamed, M.B.; Al-Maadeed, M.A.A. Stretchable quaternary phasic PVDF-HFP nanocomposite films containing graphene-titania-$SrTiO_3$ for mechanical energy harvesting. *Emergent Mater.* **2018**, *1*, 55–65. [CrossRef]
26. Serban, B.C.; Buiu, O.; Cobianu, C.; Avramescu, V.; Dumbravescu, N. Quaternary Oxidized Carbon Nanohorns–Based Nanohybrid for Resistive Humidity Sensors. EPO Patent nr. EP20465581.5, 13 November 2020.
27. Imam, S.A.; Choudhary, A.; Sachan, V.K. Design Issues for Wireless Sensor Networks and Smart Humidity Sensors for Precision Agriculture: A Review. In *2015 International Conference on Soft Computing Techniques and Implementations (ICSCTI)*; IEEE: New York, NY, USA, 2015; pp. 181–187.
28. Cobianu, C.; Serban, B.; Mihaila, M.N. Differential resonant sensor apparatus and method for detecting relative humidity. U.S. Patent 8,479,560, 2013.
29. Blank, T.A.; Eksperiandova, L.P.; Belikov, K.N. Recent trends of ceramic humidity sensors development: A review. *Sens. Actuators B Chem.* **2016**, *228*, 416–442. [CrossRef]

30. Najeeb, M.A.; Ahmad, Z.; Shakoor, R.A. Organic thin-film capacitive and resistive humidity sensors: A focus review. *Adv. Mater. Interfaces* **2018**, *5*, 1800969. [CrossRef]
31. Serban, B.C.; Buiu, O.; Dumbravescu, N.; Cobianu, C.; Avramescu, V.; Brezeanu, M.; Nicolescu, C.M. Optimization of Sensing Layers Selection Process for Relative Humidity Sensors. *Sci. Technol.* **2020**, *23*, 93–104.
32. Farahani, H.; Wagiran, R.; Hamidon, M.N. Humidity sensors principle, mechanism, and fabrication technologies: A comprehensive review. *Sensors* **2014**, *14*, 7881–7939. [CrossRef]
33. Björkqvist, M.; Salonen, J.; Paski, J.; Laine, E. Characterization of thermally carbonized porous silicon humidity sensor. *Sens. Actuators A Phys.* **2004**, *112*, 244–247. [CrossRef]
34. Connolly, E.J.; O'Halloran, G.M.; Pham, H.T.M.; Sarro, P.M.; French, P.J. Comparison of porous silicon, porous polysilicon and porous silicon carbide as materials for humidity sensing applications. *Sens. Actuators A Phys.* **2002**, *99*, 25–30. [CrossRef]
35. Li, G.Y.; Ma, J.; Peng, G.; Chen, W.; Chu, Z.Y.; Li, Y.H.; Li, X.D. Room-temperature humidity-sensing performance of SiC nanopaper. *ACS Appl. Mater. Interfaces* **2014**, *6*, 22673–22679. [CrossRef] [PubMed]
36. Parthibavarman, M.; Hariharan, V.; Sekar, C.J.M.S. High-sensitivity humidity sensor based on SnO_2 nanoparticles synthesized by microwave irradiation method. *Mater. Sci. Eng. C* **2011**, *31*, 840–844. [CrossRef]
37. Ates, T.; Tatar, C.; Yakuphanoglu, F. Preparation of semiconductor ZnO powders by sol–gel method: Humidity sensors. *Sens. Actuators A Phys.* **2013**, *190*, 153–160. [CrossRef]
38. Montesperelli, G.; Pumo, A.; Traversa, E.; Bearzotti, A.; Montenero, A.; Gnappi, G. Sol–gel processed TiO_2-based thin films as innovative humidity sensors. *Sens. Actuators B Chem.* **1995**, *25*, 705–709. [CrossRef]
39. Kulkarni, M.V.; Apte, S.K.; Naik, S.D.; Ambekar, J.D.; Kale, B.B. Ink-jet printed conducting polyaniline based flexible humidity sensor. *Sens. Actuators B Chem.* **2013**, *178*, 140–143. [CrossRef]
40. Kang, T.G.; Park, J.K.; Yun, G.H.; Choi, H.H.; Lee, H.J.; Yook, J.G. A real-time humidity sensor based on a microwave oscillator with conducting polymer PEDOT: PSS film. *Sens. Actuators B Chem.* **2019**, *282*, 145–151. [CrossRef]
41. Zhao, J.; Li, N.; Yu, H.; Wei, Z.; Liao, M.; Chen, P.; Zhang, G. Highly sensitive MoS_2 humidity sensors array for noncontact sensation. *Adv. Mater.* **2017**, *29*, 1702076. [CrossRef]
42. Dai, J.; Zhao, H.; Lin, X.; Liu, S.; Liu, Y.; Liu, X.; Zhang, T. Ultrafast response polyelectrolyte humidity sensor for respiration monitoring. *ACS Appl. Mater. Interfaces* **2019**, *11*, 6483–6490. [CrossRef]
43. Lv, X.; Li, Y.; Li, P.; Yang, M. A resistive-type humidity sensor based on crosslinked polyelectrolyte prepared by UV irradiation. *Sens. Actuators B Chem.* **2009**, *135*, 581–586. [CrossRef]
44. Li, Y.; Li, P.; Yang, M.; Lei, S.; Chen, Y.; Guo, X. A surface acoustic wave humidity sensor based on electrosprayed silicon-containing polyelectrolyte. *Sens. Actuators B Chem.* **2010**, *145*, 516–520. [CrossRef]
45. Viviani, M.; Buscaglia, M.T.; Buscaglia, V.; Leoni, M.; Nanni, P. Barium perovskites as humidity sensing materials. *J. Eur. Ceram. Soc.* **2001**, *21*, 1981–1984. [CrossRef]
46. Josephine, B.A.; Manikandan, A.; Teresita, V.M.; Antony, S.A. Fundamental study of $LaMg_x\ Cr_{1-x}\ O_{3-\delta}$ perovskites nano-photocatalysts: Sol-gel synthesis, characterization and humidity sensing. *Korean J. Chem. Eng.* **2016**, *33*, 1590–1598. [CrossRef]
47. Rajmohan, S.; Manikandan, A.; Jeseentharani, V.; Arul Antony, S.; Pragasam, J. Simple Co-Precipitation Synthesis and Characterization Studies of $La_{1-x}Ni_x\ VO_3$ Perovskites Nanostructures for Humidity Sensing Applications. *J. Nanosci. Nanotechnol.* **2016**, *16*, 1650–1655. [CrossRef] [PubMed]
48. Liu, J.; Sun, F.; Zhang, F.; Wang, Z.; Zhang, R.; Wang, C.; Qiu, S. In situ growth of continuous thin metal–organic framework film for capacitive humidity sensing. *J. Mater. Chem.* **2011**, *21*, 3775–3778. [CrossRef]
49. Chen, W.P.; Zhao, Z.G.; Liu, X.W.; Zhang, Z.X.; Suo, C.G. A capacitive humidity sensor based on multi-wall carbon nanotubes (MWCNTs). *Sensors* **2009**, *9*, 7431–7444. [CrossRef]
50. Han, J.W.; Kim, B.; Li, J.; Meyyappan, M. Carbon nanotube based humidity sensor on cellulose paper. *J. Phys. Chem. C* **2012**, *116*, 22094–22097. [CrossRef]
51. Zhang, X.; Ming, H.; Liu, R.; Han, X.; Kang, Z.; Liu, Y.; Zhang, Y. Highly sensitive humidity sensing properties of carbon quantum dots films. *Mater. Res. Bull.* **2013**, *48*, 790–794. [CrossRef]
52. Chaudhary, P.; Maurya, D.K.; Yadav, S.; Pandey, A.; Tripathi, R.K.; Yadav, B.C. Ultrafast responsive humidity sensor based on roasted gram derived carbon quantum dots: Experimental and theoretical study. *Sens. Actuators B Chem.* **2021**, *329*, 129116. [CrossRef]
53. Li, X.; Chen, X.; Yu, X.; Chen, X.; Ding, X.; Zhao, X. A high-sensitive humidity sensor based on water-soluble composite material of fullerene and graphene oxide. *IEEE Sens. J.* **2017**, *18*, 962–966. [CrossRef]
54. Radeva, E.; Georgiev, V.; Spassov, L.; Koprinarov, N.; Kanev, S. Humidity adsorptive properties of thin fullerene layers studied by means of quartz micro-balance. *Sens. Actuators B Chem.* **1997**, *42*, 11–13. [CrossRef]
55. Chen, M.C.; Hsu, C.L.; Hsueh, T.J. Fabrication of humidity sensor based on bilayer graphene. *IEEE Electron. Device Lett.* **2014**, *35*, 590–592. [CrossRef]
56. Zhang, D.; Chang, H.; Li, P.; Liu, R.; Xue, Q. Fabrication and characterization of an ultrasensitive humidity sensor based on metal oxide/graphene hybrid nanocomposite. *Sens. Actuators B Chem.* **2016**, *225*, 233–240. [CrossRef]
57. Zeineb, B.A.; Zhang, K.; Baillargeat, D.; Zhang, Q. Enhancement of humidity sensitivity of graphene through functionalization with polyethylenimine. *Appl Phys. Lett.* **2016**, *107*, 134102. [CrossRef]

58. Le, X.; Wang, X.; Pang, J.; Liu, Y.; Fang, B.; Xu, Z.; Gao, C.; Xu, Y.; Xie, J. A high performance humidity sensor based on surface acoustic wave and graphene oxide on AlN/Si layered structure. *Sens. Actuators B Chem.* **2018**, *255*, 2454–2461. [CrossRef]
59. Nufer, S.; Fantanas, D.; Ogilvie, S.P.; Large, M.J.; Winterauer, D.J.; Salvage, J.P.; Dalton, A.B. Percolating metallic structures templated on laser-deposited carbon nanofoams derived from graphene oxide: Applications in humidity sensing. *ACS Appl. Nano Mater.* **2018**, *1*, 1828–1835. [CrossRef]
60. Șerban, B.C.; Buiu, O.; Cobianu, C.; Marinescu, M.R. New Sensitive Layer for Relative Humidity Sensor and Its Manufacturing Method. Official Bulletin of Industrial Property Patents Section RO 134519 A2, 30 October 2020.
61. Șerban, B.C.; Buiu, O.; Cobianu, C.; Avramescu, V.R.; Marinescu, M.R. Humidity Sensor. Official Bulletin of Industrial Property Patents Section RO 134520 A2, 30 October 2020.
62. Șerban, B.C.; Buiu, O.; Cobianu, C.; Marinescu, M.R. New Chemiresistive Sensor for Humidity Detection. Official Bulletin of Industrial Property Patents Section RO 134521 A2, 30 October 2020.
63. Șerban, B.C.; Buiu, O.; Cobianu, C.; Marinescu, M.R. Sensitive Layer for Humidity Sensor with Surface Acoustic Waves. Official Bulletin of Industrial Property Patents Section RO 134499 A2, 30 October 2020.
64. Phan, D.T.; Chung, G.S. Effects of rapid thermal annealing on humidity sensor based on graphene oxide thin films. *Sens. Actuators B Chem.* **2015**, *220*, 1050–1055. [CrossRef]
65. Șerban, B.C.; Buiu, O.; Cobianu, C.; Avramescu, V.; Dumbrăvescu, N.; Brezeanu, M.; Marinescu, R. Ternary Carbon-Based Nanocomposite as Sensing Layer for Resistive Humidity Sensor. *Multidiscip. Digit. Publ. Inst. Proc.* **2019**, *29*, 114. [CrossRef]
66. Selvam, K.P.; Nakagawa, T.; Marui, T.; Inoue, H.; Nishikawa, T.; Hayashi, Y. Synthesis of solvent-free conductive and flexible cellulose–carbon nanohorn sheets and their application as a water vapor sensor. *Mater. Res. Express* **2020**, *7*, 056402. [CrossRef]
67. Serban, B.C.; Buiu, O.; Dumbravescu, N.; Cobianu, C.; Avramescu, V.; Brezeanu, M.; Nicolescu, C.M. Oxidized Carbon Nanohorns as Novel Sensing Layer for Resistive Humidity Sensor. *Acta Chim. Slov.* **2020**, *67*, 1–7. [CrossRef]
68. Serban, B.C.; Bumbac, M.; Buiu, O.; Cobianu, C.; Brezeanu, M.; Nicolescu, C. Carbon nanohorns and their nanocomposites: Synthesis, properties and applications. A concise review. *Ann. Acad. Rom. Sci. Ser. Math. Appl.* **2018**, *11*, 5–18.
69. Serban, B.C.; Buiu, O.; Dumbravescu, N.; Cobianu, C.; Avramescu, V.; Brezeanu, M.; Bumbac, M.; Pachiu, C.; Nicolescu, C.M. Oxidized Carbon Nanohorn-Hydrophilic Polymer Nanocomposite as the Resistive Sensing Layer for Relative Humidity. *Anal. Lett.* **2021**, *54*, 527–540. [CrossRef]
70. Serban, B.C.; Cobianu, C.; Dumbravescu, N.; Buiu, O.; Avramescu, V.; Bumbac, M.; Brezeanu, M. Electrical Percolation Threshold in Oxidized Single Wall Carbon Nanohorn-Polyvinylpyrrolidone Nanocomposite: A Possible Application for High Sensitivity Resistive Humidity Sensor. In Proceedings of the 2020 International Semiconductor Conference (CAS), Sinaia, Romania, 7–9 October 2020; pp. 239–242.
71. Șerban, B.C.; Cobianu, C.; Buiu, O.; Dumbrăvescu, N.; Avramescu, V.; Brezeanu, M.; Marinescu, M.R. Ternary oxidized carbon nanohorn-based nanohybrid as sensing layer for resistive humidity sensor. In Proceedings of the 3rd International Conference on Emerging Technologies in Materials Engineering, Bucharest, Romania, 29–30 October 2020; p. 83.
72. Șerban, B.C.; Cobianu, C.; Buiu, O.; Dumbrăvescu, N.; Avramescu, V.; Brezeanu, M.; Marinescu, M.R. Ternary hydrophilic carbon nanohorn/ZnO/PVP nanohybrid structure for room temperature resistive humidity sensing. In Proceedings of the 3rd International Conference on Emerging Technologies in Materials Engineering, Bucharest, Romania, 29–30 October 2020; p. 84.
73. Zhu, Y.; Murali, S.; Cai, W.; Li, X.; Suk, J.W.; Potts, J.R.; Ruoff, R.S. Graphene and graphene oxide: Synthesis, properties, and applications. *Adv. Mater.* **2010**, *22*, 3906–3924. [CrossRef] [PubMed]
74. Wagner, T.; Kohl, C.D.; Fröba, M.; Tiemann, M. Gas sensing properties of ordered mesoporous SnO_2. *Sensors* **2006**, *6*, 318–323. [CrossRef]
75. Azmer, M.I.; Zafar, Q.; Ahmad, Z.; Sulaiman, K. Humidity sensor based on electrospun MEH-PPV: PVP microstructured composite. *RSC Adv.* **2016**, *6*, 35387–35393. [CrossRef]
76. Sensirion Digital Humidity Sensor SHTC1 (RH/T) Designed for High-Volume Consumer Electronics Applications. Available online: https://www.sensirion.com/en/environmental-sensors/humidity-sensors/digital-humidity-sensor-for-consumer-electronics-and-iot/ (accessed on 17 April 2021).
77. Tan, X.; Wu, X.; Hu, Z.; Ma, D.; Shi, Z. Synthesis and catalytic activity of palladium supported on heteroatom doped single-wall carbon nanohorns. *RSC Adv.* **2017**, *7*, 29985–29991. [CrossRef]
78. Stobinski, L.; Lesiak, B.; Malolepszy, A.; Mazurkiewicz, M.; Mierzwa, B.; Zemek, J.; Bieloshapka, I. Graphene oxide and reduced graphene oxide studied by the XRD, TEM and electron spectroscopy methods. *J. Electron. Spectrosc. Relat. Phenom.* **2014**, *195*, 145–154. [CrossRef]
79. Li, X.-G.; Kresse, I.; Springer, J.; Nissen, J.; Yang, Y.-L. Morphology and gas perm selectivity of blend membranes of polyvinylpyridine with ethylcellulose. *Polymer* **2001**, *42*, 6859–6869. [CrossRef]
80. Patterson, A.L. The Scherrer Formula for X-Ray Particle Size Determination. *Phys. Rev.* **1939**, *56*, 978–982. [CrossRef]
81. Kumar, V.; Singh, S. Improved structure stability, optical and magnetic properties of Ca and Ti co-substituted BiFeO3 nanoparticles. *Appl. Surf. Sci.* **2016**, *386*, 78–83. [CrossRef]
82. López-Díaz, D.; Delgado-Notario, J.A.; Clericò, V.; Diez, E.; Merchán, M.D.; Velázquez, M.M. Towards understanding the Raman Spectrum of Graphene oxide: The effect of the chemical composition. *Coatings* **2020**, *10*, 524. [CrossRef]

83. Cobianu, C.; Serban, B.C.; Dumbravescu, N.; Buiu, O.; Avramescu, V.; Pachiu, C.; Cobianu, C. Organic–Inorganic Ternary Nanohybrids of Single-Walled Carbon Nanohorns for Room Temperature Chemiresistive Ethanol Detection. *Nanomaterials* **2020**, *10*, 2552. [CrossRef] [PubMed]
84. Shimada, T.; Sugai, T.; Fantini, C.; Souza, M.; Cançado, L.G.; Jorio, A.; Shinohara, H. Origin of the 2450 cm^{-1} Raman bands in HOPG, single-wall and double-wall carbon nanotubes. *Carbon* **2005**, *43*, 1049–1054. [CrossRef]
85. Borini, S.; White, R.; Wei, D.; Astley, M.; Haque, S.; Spigone, E.; Ryhanen, T. Ultrafast graphene oxide humidity sensors. *ACS Nano* **2013**, *7*, 11166–11173. [CrossRef]
86. Zhang, D.; Tong, J.; Xia, B. Humidity-sensing properties of chemically reduced graphene oxide/polymer nanocomposite film sensor on layer-by-layer nano self-assembly. *Sens. Actuators B Chem.* **2014**, *197*, 66–72. [CrossRef]
87. Pearson, R.G. Hard and soft acids and bases, HSAB, part 1: Fundamental principles. *J. Chem. Educ.* **1968**, *45*, 581. [CrossRef]
88. Serban, B.C.; Brezeanu, M.; Cobianu, C.; Costea, S.; Buiu, O.; Stratulat, A.; Varachiu, N. Materials selection for gas sensing. An HSAB perspective. In Proceedings of the 2014 International Semiconductor Conference (CAS), Sinaia, Romania, 13–15 October 2014; pp. 21–30.
89. Serban, B.C.; Buiu, O.; Cobianu, C.; Brezeanu, M.; Bumbac, M.; Nicolescu, C.M. Nanostructured semiconducting metal oxides for ammonia sensors. A novel HSAB sensing paradigm. *Acta Chim. Slov.* **2018**, *65*, 1014–1021. [CrossRef] [PubMed]
90. Santra, S.; Hu, G.; Howe, R.C.T.; De Luca, A.; Ali, S.Z.; Udrea, F.; Hasan, T. CMOS integration of inkjet-printed graphene for humidity sensing. *Sci. Rep.* **2015**, *5*, 17374. [CrossRef] [PubMed]
91. Kuang, Q.; Lao, C.; Wang, Z.L.; Xie, Z.; Zheng, L. High-sensitivity humidity sensor based on a single SnO_2 nanowire. *J. Am. Chem. Soc.* **2007**, *129*, 6070–6071. [CrossRef]